Perforated membrane-type acoustic metamaterials

F. Langfeldt[a,*], H. Kemsies[a], W. Gleine[a], O. von Estorff[b]

[a] *Department of Automotive and Aeronautical Engineering, Hamburg University of Applied Sciences, Berliner Tor 9, D–20099 Hamburg, Germany*
[b] *Institute of Modelling and Computation, Hamburg University of Technology, Denickestr. 17, D–21073 Hamburg, Germany*

Abstract

This letter introduces a modified design of membrane-type acoustic metamaterials (MAMs) with a ring mass and a perforation so that an airflow through the membrane is enabled. Simplified analytical investigations of the perforated MAM (PMAM) indicate that the perforation introduces a second anti-resonance, where the effective surface mass density of the PMAM is much higher than the static value. The theoretical results are validated using impedance tube measurements, indicating good agreement between the theoretical predictions and the measured data. The anti-resonances yield high low-frequency sound transmission loss values with peak values over 25 dB higher than the corresponding mass-law.

Keywords: metamaterial, membrane, transmission loss, acoustic, perforated, effective mass

1. Introduction

Similar to their electromagnetic counterparts [1], acoustic metamaterials are novel kinds of structures specifically engineered to exhibit unusual and generally frequency dependent effective values of their constituent quantities mass density ρ and bulk modulus κ [2, 3]. Many different realizations of acoustic metama-

*Corresponding author. Tel.: +49 40 42875 7977
Email addresses: Felix.Langfeldt@haw-hamburg.de (F. Langfeldt), Hannes.Kemsies@haw-hamburg.de (H. Kemsies), Wolfgang.Gleine@haw-hamburg.de (W. Gleine), estorff@tu-harburg.de (O. von Estorff)

Post-print submitted to Physics Letters A *February 14, 2017*

Please cite as: Langfeldt, F., Kemsies, H., Gleine, W. and O. von Estorff. Perforated membrane-type acoustic metamaterials. *Physics Letters A* 381(16) (2017): 1457–1462. https://doi.org/10.1016/j.physleta.2017.02.036

terials have been developed in the past, including metamaterials with negative effective density [4–9], negative effective bulk modulus [10–12], double negative metamaterials [13–16], and density-near-zero metamaterials [17]. These realizations opened up new developments of acoustic devices with extraordinary capabilities, such as acoustic superlenses for focusing of sound waves below the diffraction limit [18, 19], acoustic cloaks [20–23], perfect acoustic absorbers [24–26], and low-frequency sound barriers [4, 6, 27–29]. In particular, the latter application of acoustic metamaterials is very promising for many fields of noise control where most conventional noise protection materials are governed by the so-called mass law. The mass-law relates the sound transmission loss TL to the surface mass density of the material m'' via $\mathrm{TL} = 20\log_{10}[\omega m''/(2Z_0)]$, where $\omega = 2\pi f$ is the angular frequency and Z_0 the characteristic impedance of the surrounding fluid, indicating the poor low-frequency performance of mass-law governed structures [30]. From the low-frequency metamaterial sound barriers available in the literature, the membrane-type acoustic metamaterials (MAMs), originally proposed by Yang et al. [6], stand out due to their compact and lightweight design: MAMs consist of a thin prestressed membrane with small rigid masses attached to it and a total surface mass density typically smaller than $2\,\mathrm{kg/m^2}$. At low frequencies these structures exhibit frequency bands around certain anti-resonance frequencies with negative effective mass density and large TL values that can exceed the corresponding mass-law transmission loss considerably [6, 31]. This extraordinary low-frequency sound insulation capability of MAMs makes them specifically appealing for noise control devices with strict boundaries for the overall weight and size.

For a MAM, the anti-resonance frequencies can be easily tuned by selecting suitable combinations of the added masses and the membrane prestress [32]. However, the frequency bands with large TL values typically are very narrow. Therefore, a special treatment is required to achieve broadband noise insulation with MAMs, such as stacking multiple MAM layers [28, 33] or multiple added masses per unit cell [24, 34]. Nevertheless, the stacked arrangement of MAMs and the addition of extra masses increase the total mass of the noise shield, possibly degrading the lightweight properties of MAMs. This approach also increases the level of complexity, impacting an easy fabrication of such structures.

This letter presents a new kind of MAM with perforations to introduce additional anti-resonances. Experimental and theoretical methods are employed to study the acoustical properties of these perforated MAMs (PMAMs). The basic structure of a PMAM unit cell is shown in Fig. 1(a). It consists of a rectangular membrane with equal edge lengths L (other membrane shapes, e.g. circular, are also possible) and a rigid ring mass added to the membrane. At the inner diameter of the ring mass the membrane material is open allowing air particles to pass through the circular channel which is formed by the ring mass. As shown in the cross-sectional view in Fig. 1(b), the ring mass, similar to the neck of a Helmholtz resonator [35], confines a small air volume which acoustically acts like an additional mass. The resulting vibrational amplitude of the fluid volume inside the perforation is denoted with $\hat{w}_0$, while the membrane displacement amplitude is given by $\hat{w}_m$. For perforation diameters much larger than the acoustic boundary layer thickness it is assumed that the viscous coupling between the fluid volume and the ring mass is comparatively weak, so that the displacement amplitude of the air volume can be considerably different than the displacement amplitude of the ring mass. Since no mass is added, this

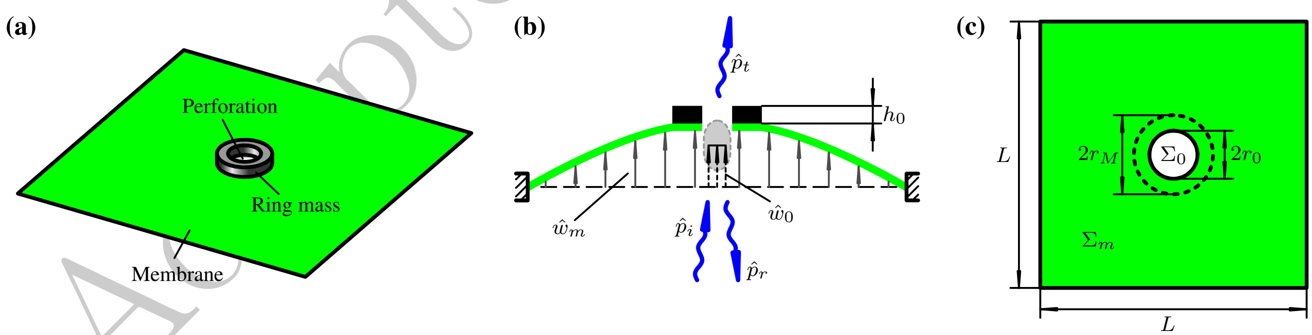

Figure 1: Schematic representation of the proposed perforated MAM (PMAM) unit cell. (a) Isometric view of a PMAM with added ring mass; (b) Displacement amplitudes of the MAM and the air volume inside the perforation; (c) Definition of the surface parts on the PMAM unit cell.

approach offers a weight efficient alternative to previous strategies for enhancing the bandwidth of MAMs.

2. Theory

The normal incidence sound transmission factor $t = \hat{p}_t/\hat{p}_i$ of the proposed PMAM unit cell is obtained analytically by calculating the effective surface mass density $\tilde{m}''$ of the structure. This quantity can be defined in analogy to Newton's second law as $\tilde{m}'' = \langle \Delta\hat{p}\rangle_\Sigma / \langle \hat{a}\rangle_\Sigma$ [6], where $\Delta\hat{p}$ is the pressure amplitude difference across both sides of the PMAM and $\hat{a}$ is the surface normal acceleration amplitude. $\langle \cdots \rangle_\Sigma$ denotes the surface average of a quantity along the whole PMAM surface Σ which is given by the union of the MAM surface Σ_m and the cross section of the perforation Σ_0 (i.e. $\Sigma = \Sigma_m \cup \Sigma_0$, see Fig. 1(c)). Normally incident waves are considered, which means that the pressure amplitude difference $\Delta\hat{p}$ is uniform, i.e. $\langle \Delta\hat{p}\rangle_\Sigma = \Delta\hat{p}$. The time dependence of the acoustic pressure fields and the MAM vibration is harmonic. Therefore, the acceleration amplitude can be expressed in terms of the displacement amplitude as $\hat{a} = -\omega^2 \hat{w}$. Furthermore, since Σ is composed of Σ_m and Σ_0, the surface average of $\hat{w}$ can be split up into two parts with $\langle \hat{w}\rangle_\Sigma = (1-\sigma_0)\langle \hat{w}_m\rangle_{\Sigma_m} + \sigma_0 \langle \hat{w}_0\rangle_{\Sigma_0}$, where $\sigma_0 = \pi r_0^2/L^2$ is the perforation ratio and r_0 is the radius of the perforation. This yields the following expression for calculating the effective surface mass density of the PMAM

$$\tilde{m}'' = \frac{\Delta\hat{p}}{-\omega^2\left[(1-\sigma_0)\langle \hat{w}_m\rangle_{\Sigma_m} + \sigma_0 \langle \hat{w}_0\rangle_{\Sigma_0}\right]}. \tag{1}$$

Some rearrangements and simplifications can be applied to Eq. (1) in order to obtain a more convenient expression for $\tilde{m}''$: First, the effective surface mass density of the unperforated MAM, defined as $\tilde{m}''_m = \langle \Delta\hat{p}\rangle_\Sigma / \langle \hat{a}_m\rangle_\Sigma = \Delta\hat{p}/(-\omega^2 \langle \hat{w}_m\rangle_\Sigma)$ is introduced. This quantity can be readily obtained from measurements, numerical simulations, or analytical models of MAMs (e.g. [36, 37]). With $\langle \hat{w}_m\rangle_\Sigma = (1-\sigma_0)\langle \hat{w}_m\rangle_{\Sigma_m} + \sigma_0 \langle \hat{w}_m\rangle_{\Sigma_0}$ this leads to

$$\tilde{m}'' = \frac{1}{1/\tilde{m}''_m - \sigma_0\omega^2 \langle \hat{w}_0 - \hat{w}_m\rangle_{\Sigma_0}/\Delta\hat{p}}. \tag{2}$$

The ring mass is relatively heavy compared to the mass of the air volume enclosed inside the perforation and it is fixed to the membrane material. Therefore, it can be expected that along the relatively small perforation surface $\hat{w}_m \ll \hat{w}_0$ for most frequencies, except around the resonance frequencies of the MAM, where the mass displacement can become quite large. Thus, denoting the surface average of the particle displacement amplitude inside the hole by $\bar{w}_0$, Eq. (2) is simplified to

$$\tilde{m}'' = \frac{1}{1/\tilde{m}''_m - \sigma_0 \omega^2 \bar{w}_0 / \Delta\hat{p}}. \tag{3}$$

Careful inspection of Eq. (3) reveals that the effective surface mass density of the PMAM can be understood as a parallel assembly of two individual effective surface mass densities. These are the effective surface mass densities of the MAM $\tilde{m}''_m$ and the perforation with the MAM fixed $\tilde{m}''_0 = \Delta\hat{p}/(-\sigma_0 \omega^2 \bar{w}_0)$:

$$\frac{1}{\tilde{m}''} = \frac{1}{\tilde{m}''_m} + \frac{1}{\tilde{m}''_0} \quad \text{or} \quad \tilde{m}'' = \frac{\tilde{m}''_m \tilde{m}''_0}{\tilde{m}''_m + \tilde{m}''_0}. \tag{4}$$

The relationship in Eq. (4) indicates that if the magnitudes of $\tilde{m}''_m$ and $\tilde{m}''_0$ are substantially different (for example at the MAM anti-resonance frequency, where $\tilde{m}''_m \to \infty$) the lower surface mass density dominates the sound transmission through the PMAM. This can be explained by the fact that acoustic waves prefer to follow the sound path with the least resistance, similar to sound waves bypassing a solid object through small gaps. However, if $\tilde{m}''_m$ and $\tilde{m}''_0$ are similar in magnitude, the mutual acoustic interaction between the MAM and the perforation can lead to very large effective surface mass densities of the PMAM. When both $\tilde{m}''_m$ and $\tilde{m}''_0$ are equal in magnitude and have opposite signs, the denominator in Eq. (4) vanishes and $\tilde{m}''$ goes to infinity. This can be explained physically as follows: If $\tilde{m}''_0 = -\tilde{m}''_m$, then it follows from the definitions of the effective surface mass densities that $\tilde{m}''_0 = \Delta\hat{p}/(-\sigma_0 \omega^2 \bar{w}_0) = -\Delta\hat{p}/(-\omega^2 \langle \hat{w}_m \rangle_\Sigma) = -\tilde{m}''_m$. Using the perforation ratio σ_0, this expression can be reformulated as $\pi r_0^2 \bar{w}_0 = -L^2 \langle \hat{w}_m \rangle_\Sigma$. This shows that, for a given uniform $\Delta\hat{p}$, $\tilde{m}'' \to \infty$ when the air volume squeezed through the perforation is exactly equal to the air volume displaced by the MAM in the opposite direction. The MAM vibration and the vibration of the fluid inside the perforation are out of phase by 180° and the net displaced fluid volume becomes zero. Hence, instead of being radiated into the far field, the sound energy is trapped inside an acoustic near field. In this near field the pressure difference $\Delta\hat{p}$ between both sides of the metamaterial is compensated by a dynamic airflow through the perforation. A similar effect has already been observed in the case of MAMs with ventilated surroundings [26, 38, 39]. In the present case, however, this effect is realized by perforating the membrane material itself without requiring a specifically designed frame structure.

3. Results

Analytical calculations of the effective surface mass density $\tilde{m}''$ of a PMAM with an edge length of $L = 46$ mm have been carried out using the relation given in Eq. (4). It should be mentioned that Eq. (4) has been derived under the assumption that the vibration amplitude of the membrane material is much smaller than the particle displacement inside the perforation. As discussed in the previous section, this assumption is reasonable for most frequencies, except for the resonance frequencies of the MAM. Thus, Eq. (4) must be used with care in the vicinity of these frequencies. However, in the following analysis the $\tilde{m}''$ of the PMAM will also be evaluated at the MAM resonance frequencies in order to quantify how strict this limitation is by comparison with experimental data.

The membrane material of the PMAM sample is Oracover, an iron-on film with a surface mass density of $m''_m = 103$ g/m^2 and a prestress of 210 N/m. As shown in Fig. 1, a steel ring mass with an outer radius of $r_M = 3$ mm, inner radius $r_0 = 1.5$ mm, and thickness $h_0 = 2$ mm (thus, the added mass equals to $M = 333$ mg) is attached to the center of the rectangular membrane. The total surface mass density of the metamaterial is given by $m''_{\text{tot}} = m''_m + M/L^2 = 260$ g/m^2. As mentioned above, the membrane is perforated across the inner cross-section of the ring mass to create the proposed PMAM and the resulting perforation ratio is $\sigma_0 = 0.33\%$. The material properties of the ambient air are given by $\rho_0 = 1.225$ kg/m^3 for the density, $c_0 = 340$ m/s for the speed of sound, and $\eta_0 = 18.1$ µPa s for the dynamic viscosity.

The effective surface mass density of the unperforated MAM $\tilde{m}''_m$ has been calculated using an analytical model for MAMs with general mass shapes [37]. $\tilde{m}''_0$ can be expressed in terms of the hole impedance $\mathcal{Z}_0 = \mathcal{R}_0 + \mathrm{i}\omega\mathcal{M}_0 = \Delta\hat{p}/(\mathrm{i}\omega\bar{w}_0)$ as $\tilde{m}''_0 = \mathcal{Z}_0/(\sigma_0 \mathrm{i}\omega)$, where $\mathcal{R}_0$ denotes the resistance due to the viscosity of the air and $\omega\mathcal{M}_0$ denotes the mass reactance of the fluid inside the hole. Analytical expressions for $\mathcal{R}_0$ and $\mathcal{M}_0$ are available in the literature, e.g. [40], where

$$\mathcal{R}_0 = \frac{8\eta_0 h_0}{r_0^2}\left(\sqrt{1+\frac{X^2}{32}} + \frac{\sqrt{2}Xr_0}{16h_0}\right) \tag{5}$$

and

$$\mathcal{M}_0 = \rho_0 h_0 \left(1 + \frac{1}{\sqrt{9+0.5X^2}} + 1.7\frac{r_0}{h_0}\right), \tag{6}$$

with the perforate constant $X = r_0\sqrt{\rho_0\omega/\eta_0}$. It can be seen that $\mathcal{M}_0$ is proportional to the hole length h_0 (corresponding to the thickness of the ring mass) and linearly dependent on the normalized hole radius r_0/h_0. Thus, by adjusting these geometrical parameters, the inertia of the perforation fluid volume can be easily modified.

The analytical results for the effective surface mass densities of the unperforated MAM $\tilde{m}''_m$, the perforation $\tilde{m}''_0$, and PMAM $\tilde{m}''$ are shown in Fig. 2, with the magnitudes and phase angles given in Figs. 2(a) and 2(b), respectively. Additionally, the frequency bands with positive (PB) and negative (NB) effective surface mass density are indicated for the MAM and PMAM in Fig. 2(c). These frequency bands have been identified by evaluating the phase angle shown in Fig. 2(b): Phase angles of $-\frac{\pi}{2}\ldots 0$ correspond to a positive real part of the effective surface mass density and thus are attributed to the PB bands. Phase angles from $-\pi$ to $-\frac{\pi}{2}$, on the other hand, yield a negative real part and therefore correspond to the NB bands. The thin dotted line in Fig. 2(b) indicates the boundary between the PB and NB bands.

The absolute value of $\tilde{m}''_m$ in Fig. 2(a) follows the well-known qualitative behavior of the effective surface mass density of MAMs [36] with two visible

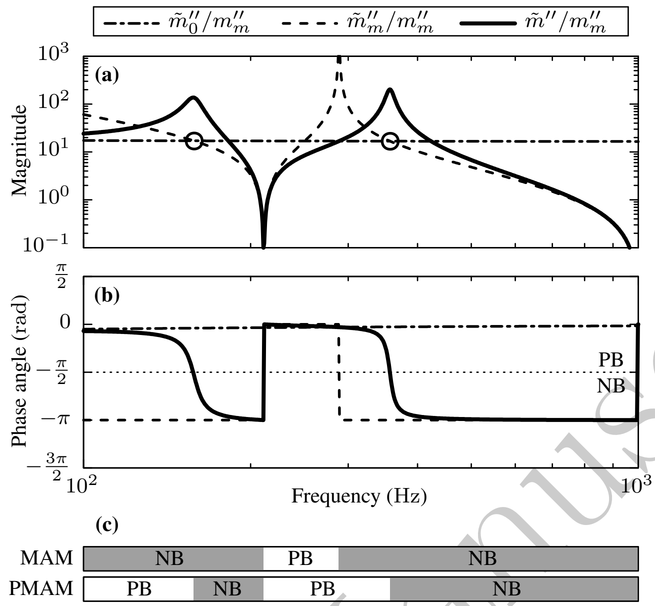

Figure 2: Effective surface mass density of the PMAM $\tilde{m}''$, the unperforated MAM $\tilde{m}''_m$, and the perforation fluid volume $\tilde{m}''_0$ normalized by the surface mass density of the membrane material m''_m. (a) Magnitude; (b) Phase angle; (c) Frequency bands with positive (PB) and negative (NB) effective surface mass density.

resonances, where $|\tilde{m}''_m| \to 0$, and an anti-resonance in between, where $|\tilde{m}''_m| \to \infty$. Due to the negligible damping in the given membrane material, the phase of $\tilde{m}''_m$ undergoes rapid changes from $-\pi$ to 0 at the first resonance frequency and back from 0 to $-\pi$ at the anti-resonance. The surface mass density of the perforation $\tilde{m}''_0$, on the other hand, is nearly independent of frequency with $\tilde{m}''_0 \approx \mathcal{M}_0/\sigma_0 \approx 1.7\,\mathrm{kg/m^2}$. The imaginary part of $\tilde{m}''_0$ is close to zero due to the negligible resistance term for the given perforation geometry and therefore $\arg \tilde{m}''_0 \approx 0$, as shown in Fig. 2(b).

In Fig. 2(a), those intersections of $|\tilde{m}''_m|$ and $|\tilde{m}''_0|$ are marked with circles, where the phase difference of those quantities is simultaneously $\approx \pi$, so that the anti-resonance condition $\tilde{m}''_m = -\tilde{m}''_0$ is fulfilled for the PMAM configuration. At these two frequencies the PMAM effective surface mass density $\tilde{m}''$ is considerably larger than $\tilde{m}''_m$ and $\tilde{m}''_0$ with two anti-resonance peaks visible in the spectrum. The maximum values at those peaks, however, are not approaching infinity, because the phase difference between $\tilde{m}''_m$ and $\tilde{m}''_0$ is not exactly π but slightly less than that since the resistance $\mathcal{R}_0$ of the perforation is non-zero. From Eq. (4) it follows that even slight deviations $\delta\phi$ from the ideal phase difference π reduce the peak magnitude value of the PMAM surface mass density to $|\tilde{m}''| \approx |\tilde{m}''_m|/|\delta\phi|$. Thus, the higher the perforation resistance $\mathcal{R}_0$, the smaller the maximum effective surface mass density at the PMAM anti-resonances. Comparing the phase angle distribution of the PMAM with that of the unperforated MAM in Fig. 2(b), it can be seen that the PMAM's $\tilde{m}''$ undergoes a much smoother phase change at the anti-resonance frequencies than $\tilde{m}''_m$ at the MAM anti-resonance. This can also be attributed to the resistance $\mathcal{R}_0$ of the perforation: The damping due to the frictional losses in the perforation smears out the anti-resonance phase change over a certain frequency band. For the MAM's $\tilde{m}''_m$, on the other hand, a sudden phase jump is observed in Fig. 2(b), because the membrane material is assumed to be undamped.

In order to modify the two anti-resonance frequencies of the PMAM, the perforation mass reactance $\omega\mathcal{M}_0$ can be increased by increasing the perforation length h_0. Thus, the dash-dotted line in Fig. 2(a) is shifted upwards and the encircled intersections move to lower frequencies because the effective surface mass density of the unperforated MAM is unchanged. Increasing the perforation radius r_0, on the other hand, also increases the perforation mass reactance. But since the perforation ratio σ_0 is proportional to the square of r_0, $\tilde{m}''_0$ is effectively reduced when r_0 is increased. Thus, the anti-resonance frequencies will be higher for larger perforation radii, provided that the added mass magnitude M is kept constant by choosing appropriate mass geometries.

The negative effective mass band-gaps of the PMAM, as shown in Fig. 2(c), are smaller than the MAM band-gaps. The first band-gap of the unperforated MAM extends from 0 Hz to the first MAM resonance frequency. The PMAM, however, is dominated by the perforation behavior at very low frequencies, which is characterized by a positive effective surface mass density. Thus, the first band-gap of the PMAM extends only from the first anti-resonance frequency to the first MAM resonance. The extent of the second band-gap is also reduced, because the second anti-resonance of the PMAM is at a higher frequency than the MAM anti-resonance.

In order to investigate the normal incidence sound transmission of the proposed PMAM unit cell experimentally, an unperforated and a perforated MAM test sample with the same properties as given above have been measured inside an impedance tube using the 4-microphone-technique [41]. The measured results for the transmission loss $\mathrm{TL} = -20\log_{10}|t|$ and transmission factor phase are given in Figs. 3(a) and 3(b), respectively. These figures also show the predictions from the analytical model using the mass-law relationship for t with the corresponding effective surface mass densities, given by $t = (1+\mathrm{i}\omega\tilde{m}''/(2Z_0))^{-1}$. Additionally, the mass-law transmission loss of an equivalent wall with the same surface mass density as the PMAM test sample $m''_{\mathrm{tot}} = 260\,\mathrm{g/m^2}$ is given in Fig. 3(a) for comparison (gray dash-dotted line).

As can be seen in Fig. 3, the measured values and analytically predicted data agree well in both MAM and PMAM configurations. Even at the first

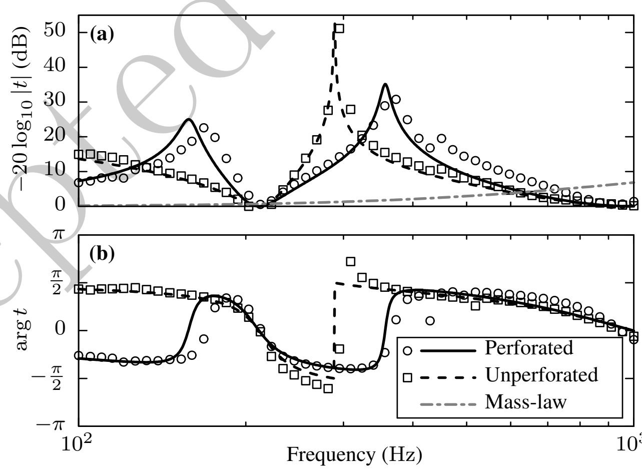

Figure 3: Analytically calculated (lines) and measured (symbols) acoustic transmission factor t of the PMAM and unperforated MAM. (a) Transmission loss $\mathrm{TL} = -20\log_{10}|t|$; (b) Transmission factor phase.

MAM resonance frequency around 200 Hz a good agreement between the theoretical calculations and the measured data can be found, despite the limited applicability of Eq. (4) at the MAM resonances. This can be attributed to the damping effect of the sound radiated by the membrane, which strongly limits the vibration amplitude of the membrane at resonance.

The anti-resonance frequencies of the PMAM are slightly underpredicted by the analytical model, which can be explained by the empirical formula (6) slightly overpredicting the air volume mass inside the perforation. As already observed in Fig. 2, the two TL peaks of the PMAM (24 dB and 34 dB) are not as high as the MAM peak (52 dB). However, at frequencies below the first MAM resonance at ≈ 200 Hz, the sound reduction of the PMAM is considerably improved over the MAM TL due to the new anti-resonance. At this peak, the PMAM TL is nearly 18 dB higher than the MAM TL.

It should be mentioned that at the very low-frequency end of the TL-spectrum shown in Fig. 3 the sound transmission loss of the PMAM becomes smaller than that of the unperforated MAM. This is caused by the sound waves passing through the perforation, which, well below the fundamental resonance frequency of the MAM, acts like a leakage to the incoming sound waves. Thus, in the limit $f \to 0$, the PMAM transmission loss approaches a constant value corresponding to the static air flow resistance of the perforation. The sound transmission through the MAM, on the other hand, becomes vanishingly small due to the stiffness-effect of the simply-supported membrane edges below the fundamental frequency. In practical applications of MAMs, however, this stiffness-controlled sound transmission regime is not particularly relevant, because the ideal simply-supported edge conditions can rarely be reproduced on large and lightweight structures [33, 42]. This should be taken into account when comparing the performance of perforated and unperforated MAMs at very low frequencies.

In order to illustrate the relationship between the two anti-resonance frequencies of the PMAM, f_{P1} and f_{P2}, and the perforation geometry (defined by h_0 and r_0), parameter studies have been performed using the theoretical model. In these calculations, the perforation length h_0 has been varied between 0 (i.e.

a vanishingly thin disc) and 10 mm (i.e. a long tube) and the perforation radius r_0 between 0 (i.e. no perforation) and 2.5 mm (i.e a very thin-walled ring mass). All other parameters have been kept the same, as described in the beginning of this section. In particular, the added mass M has been kept constant in order to emphasize the mass-neutral tunability of the PMAM anti-resonances by changing the perforation properties. In practice, a constant mass M can be achieved by choosing suitable geometrical shapes and materials for the added mass (e.g. a conical shape for increasing the perforation length).

The parameter study results are shown in Fig. 4. The solid lines represent the variation of the anti-resonance frequencies with the air viscosity $\eta_0 = 18.1$ µPa s. For comparison, the dashed lines indicate the frictionless case with $\eta_0 = 0$, so that the resistance part $\mathcal{R}_0$ in the hole impedance $\mathcal{Z}_0$ is zero. The horizontal dotted line in Fig. 4 corresponds to the anti-resonance frequency of the unperforated MAM at 290 Hz.

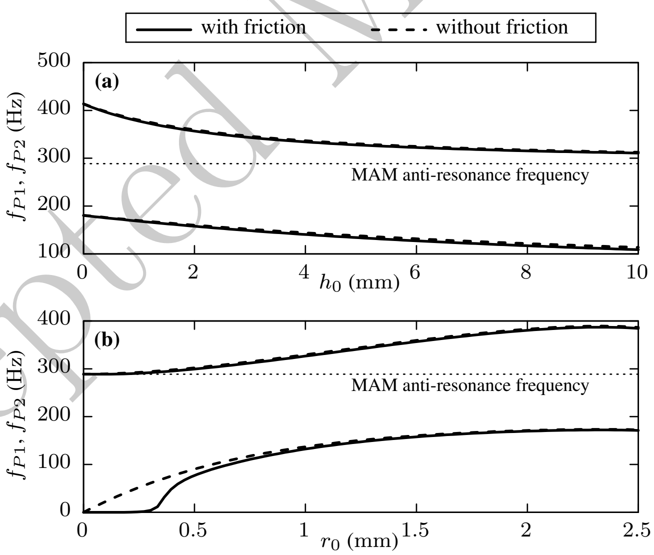

Figure 4: Relationship between the two anti-resonance frequencies of the PMAM f_{P1} and f_{P2} and the perforation geometry. All other parameters are kept constant. The dashed lines indicate results for the frictionless case with $\eta_0 = 0$. (a) Perforation length h_0; (b) Perforation radius r_0.

The relationship between the anti-resonance frequencies and the perforation length shown in Fig. 4(a) confirms the expected behavior discussed in the context of the effective surface mass density shown in Fig. 2. As h_0 increases, both anti-resonance frequencies are shifted to lower frequencies as the fluid mass $\mathcal{M}_0$ trapped inside the perforation increases according to Eq. (6). The anti-resonance frequency of the unperforated MAM serves as a lower bound for the second anti-resonance frequency of the PMAM, while f_{P1} (theoretically) approaches 0 Hz as $h_0 \to \infty$. The influence of the air viscosity on the anti-resonance frequencies is vanishingly small within the investigated range of perforation lengths, because the perforation radius $r_0 = 1.5$ mm is comparatively large so that the resistance term $\mathcal{R}_{\prime}$ is small compared to the reactance $\omega\mathcal{M}_0$.

The influence of the perforation radius r_0 on the anti-resonance frequencies is shown in Fig. 4(b). At $r_0 = 0$, the second PMAM anti-resonance frequency equals the unperforated MAM anti-resonance frequency and f_{P1} is zero. For increasing r_0, both anti-resonance frequencies become larger. As already explained in the discussion of Fig. 2, this can be attributed to the quadratically increasing perforation ratio σ_0 which effectively decreases the effective surface mass density of the perforation m_0''. An interesting observation can be made for the variation of the first anti-resonance frequency at small values of r_0: When friction inside the perforation is considered, f_{P1} remains near-zero for small perforation radii up to 0.3 mm. The curve for the frictionless case is substantially different to that in this parameter range. This observation can be attributed to the friction leading to a choking of the particle flow through the orifice when the diameter is too small. In that case, the PMAM behaves like an unperforated MAM at low frequencies, until a certain critical radius (in this case approximately 0.3 mm) is reached and the f_{P1} relationship approaches the frictionless case.

4. Conclusions

In conclusion, perforated MAMs have been investigated in this letter using analytical and experimental methods. It has been shown that the air volume inside the perforation represents an additional degree of freedom which introduces a new anti-resonance between 0 Hz and the first MAM resonance. This additional peak appears without any additional mass incorporated into the system and can be tuned by selecting suitable properties for the perforation geometry, as shown in Fig. 4. The TL at the new anti-resonance exceeds the corresponding mass-law considerably by over 25 dB. The analytical model, based upon the effective surface mass densities of the unperforated MAM and the perforation itself, showed very good agreement with the measured data. Apart from increasing the reflectivity of MAMs, PMAMs are expected to be also applicable as lightweight absorbers, e.g. backed by a closed cavity similar to a conventional Helmholtz resonator.

Acknowledgements

This work was supported by the Federal Ministry for Economic Affairs and Energy [grant number 20K1102D].

References

[1] D. R. Smith, J. B. Pendry, M. C. K. Wiltshire, Metamaterials and negative refractive index, Science 305 (2004) 788–792.

[2] S. A. Cummer, J. Christensen, A. Alù, Controlling sound with acoustic metamaterials, Nature Reviews Materials 1 (2016) 16001.

[3] G. Ma, P. Sheng, Acoustic metamaterials: From local resonances to broad horizons, Science Advances 2 (2016) 1501595.

[4] Z. Liu, X. Zhang, Y. Mao, Y. Y. Zhu, Z. Yang, C. T. Chan, P. Sheng, Locally resonant sonic materials, Science 289 (2000) 1734–1736.

[5] Z. Liu, C. T. Chan, P. Sheng, Analytic model of phononic crystals with local resonances, Phys. Rev. B 71 (2005) 014103.

[6] Z. Yang, J. Mei, M. Yang, N. H. Chan, P. Sheng, Membrane-type acoustic metamaterial with negative dynamic mass, Phys. Rev. Lett. 101 (2008) 204301.

[7] S. H. Lee, C. M. Park, Y. M. Seo, Z. G. Wang, C. K. Kim, Acoustic metamaterial with negative density, Phys. Lett. A 373 (2009) 4464–4469.

[8] Y. Xiao, J. Wen, X. Wen, Sound transmission loss of metamaterial-based thin plates with multiple subwavelength arrays of attached resonators, J. Sound Vib. 331 (2012) 5408–5423.

[9] N. Sui, X. Yan, T.-Y. Huang, J. Xu, F.-G. Yuan, Y. Jing, A lightweight yet sound-proof honeycomb acoustic metamaterial, Appl. Phys. Lett. 106 (2015) 171905.

[10] N. Fang, D. Xi, J. Xu, M. Ambati, W. Srituravanich, C. Sun, X. Zhang, Ultrasonic metamaterials with negative modulus, Nat. Mater. 5 (2006) 452–456.

[11] S. H. Lee, C. M. Park, Y. M. Seo, Z. G. Wang, C. K. Kim, Acoustic metamaterial with negative modulus., J. Phys.: Condens. Matter 21 (2009) 175704.

[12] V. García-Chocano, R. Graciá-Salgado, D. Torrent, F. Cervera, J. Sánchez-Dehesa, Quasi-two-dimensional acoustic metamaterial with negative bulk modulus, Phys. Rev. B 85 (2012) 184102.

[13] J. Li, C. T. Chan, Double-negative acoustic metamaterial, Phys. Rev. E 70 (2004) 055602.

[14] S. H. Lee, C. M. Park, Y. M. Seo, Z. G. Wang, C. K. Kim, Composite acoustic medium with simultaneously negative density and modulus, Phys. Rev. Lett. 104 (2010) 054301.

[15] M. Yang, G. Ma, Z. Yang, P. Sheng, Coupled membranes with doubly negative mass density and bulk modulus, Phys. Rev. Lett. 110 (2013) 134301.

[16] Z. Chen, C. Xue, L. Fan, S.-Y. Zhang, X.-J. Li, H. Zhang, J. Ding, A tunable acoustic metamaterial with double-negativity driven by electromagnets, Scientific Reports 6 (2016) 30254.

[17] Y. Gu, Y. Cheng, J. Wang, X. Liu, Controlling sound transmission with density-near-zero acoustic membrane network, J. Appl. Phys. 118 (2015) 024505.

[18] J. Li, L. Fok, X. Yin, G. Bartal, X. Zhang, Experimental demonstration of an acoustic magnifying hyperlens, Nat. Mater. 8 (2009) 931–934.

[19] J. J. Park, C. M. Park, K. J. B. Lee, S. H. Lee, Acoustic superlens using membrane-based metamaterials, Appl. Phys. Lett. 106 (2015) 051901.

[20] B.-I. Popa, L. Zigoneanu, S. A. Cummer, Experimental acoustic ground cloak in air, Phys. Rev. Lett. 106 (2011) 253901.

[21] S. Zhang, C. Xia, N. Fang, Broadband acoustic cloak for ultrasound waves, Phys. Rev. Lett. 106 (2011) 024301.

[22] X. Zhu, B. Liang, W. Kan, X. Zou, J. Cheng, Acoustic cloaking by a superlens with single-negative materials, Phys. Rev. Lett. 106 (2011) 014301.

[23] J. Zhao, Z. N. Chen, B. Li, C.-W. Qiu, Acoustic cloaking by extraordinary sound transmission, J. Appl. Phys. 117 (2015) 214507.

[24] J. Mei, G. Ma, M. Yang, Z. Yang, W. Wen, P. Sheng, Dark acoustic metamaterials as super absorbers for low-frequency sound, Nat. Commun. 3 (2012) 756.

[25] X. Jiang, B. Liang, R.-Q. Li, X.-Y. Zou, L.-L. Yin, J.-C. Cheng, Ultra-broadband absorption by acoustic metamaterials, Appl. Phys. Lett. 105 (2014) 243505.

[26] M. Yang, C. Meng, C. Fu, Y. Li, Z. Yang, P. Sheng, Subwavelength total acoustic absorption with degenerate resonators, Appl. Phys. Lett. 107 (2015) 104104.

[27] K. M. Ho, C. K. Cheng, Z. Yang, X. X. Zhang, P. Sheng, Broadband locally resonant sonic shields, Appl. Phys. Lett. 83 (2003) 5566–5568.

[28] Z. Yang, H. M. Dai, N. H. Chan, G. C. Ma, P. Sheng, Acoustic metamaterial panels for sound attenuation in the 50–1000 Hz regime, Appl. Phys. Lett. 96 (2010) 041906.

[29] X. Wang, H. Zhao, X. Luo, Z. Huang, Membrane-constrained acoustic metamaterials for low frequency sound insulation, Applied Physics Letters 108 (2016) 041905.

[30] F. J. Fahy, P. Gardonio, Sound and structural vibration: radiation, transmission and response, Academic press, Oxford, UK, 2007.

[31] T.-Y. Huang, C. Shen, Y. Jing, Membrane- and plate-type acoustic metamaterials, The Journal of the Acoustical Society of America 139 (2016) 3240–3250.

[32] Y. Zhang, J. Wen, Y. Xiao, X. Wen, J. Wang, Theoretical investigation of the sound attenuation of membrane-type acoustic metamaterials, Phys. Lett. A 376 (2012) 1489–1494.

[33] C. J. Naify, C.-M. Chang, G. McKnight, S. R. Nutt, Scaling of membrane-type locally resonant acoustic metamaterial arrays, J. Acous. Soc. Am. 132 (2012) 2784–2792.

[34] C. J. Naify, C.-M. Chang, G. McKnight, F. Scheulen, S. Nutt, Membrane-type metamaterials: Transmission loss of multi-celled arrays, J. Appl. Phys. 109 (2011) 104902.

[35] M. J. Crocker, Handbook of Noise and Vibration Control, John Wiley & Sons, Hoboken, New Jersey, 2007.

[36] M. Yang, G. Ma, Y. Wu, Z. Yang, P. Sheng, Homogenization scheme for acoustic metamaterials, Phys. Rev. B 89 (2014) 064309.

[37] F. Langfeldt, W. Gleine, O. von Estorff, Analytical model for low-frequency transmission loss calculation of membranes loaded with arbitrarily shaped masses, J. Sound Vib. 349 (2015) 315–329.

[38] G. Ma, M. Yang, Z. Yang, P. Sheng, Low-frequency narrow-band acoustic filter with large orifice, Appl. Phys. Lett. 103 (2013) 011903.

[39] N. Cselyuszka, M. Sečujski, V. Crnojević-Bengin, Novel negative mass density resonant metamaterial unit cell, Phys. Lett. A 379 (2015) 33–36.

[40] D.-Y. Maa, Theory and design of microperforated panel sound-absorbing constructions, Sci. Sinica 18 (1975) 55–71.

[41] American Society for Testing and Materials ASTM E2611-09, Standard test method for measurement of normal incidence sound transmission of acoustical materials based on the transfer matrix method, 2009.

[42] A. Peiffer, M. Grünewald, P. Lempereur, Comment on “A lightweight yet sound-proof honeycomb acoustic metamaterial” [Appl. Phys. Lett. 106, 171905 (2015)], Appl. Phys. Lett. 107 (2015) 216101.

Figure Captions

Figure 1 Schematic representation of the proposed perforated MAM (PMAM) unit cell. (a) Isometric view of a PMAM with added ring mass; (b) Displacement amplitudes of the MAM and the air volume inside the perforation; (c) Definition of the surface parts on the PMAM unit cell.

Figure 2 Effective surface mass density of the PMAM $\tilde{m}''$, the unperforated MAM $\tilde{m}''_m$, and the perforation fluid volume $\tilde{m}''_0$ normalized by the surface mass density of the membrane material m''_m. (a) Magnitude; (b) Phase angle; (c) Frequency bands with positive (PB) and negative (NB) effective surface mass density.

Figure 3 Analytically calculated (lines) and measured (symbols) acoustic transmission factor t of the PMAM and unperforated MAM. (a) Transmission loss $\mathrm{TL} = -20 \log_{10} |t|$; (b) Transmission factor phase.

Figure 4 Relationship between the two anti-resonance frequencies of the PMAM f_{P1} and f_{P2} and the perforation geometry. All other parameters are kept constant. The dashed lines indicate results for the frictionless case with $\eta_0 = 0$. (a) Perforation length h_0; (b) Perforation radius r_0.